Hard exclusive reactions and generalized parton distributions at HERMES

M. Düren[a] (on behalf of the HERMES collaboration)

[a]II. Phys. Inst., Univ. Giessen, Heinrich-Buff-Ring 16, 35392 Giessen, Germany

The concept of generalized parton distributions is discussed and applied to hard exclusive reactions at the HERMES experiment at DESY. Recent results on hard exclusive meson production and in particular on deeply virtual Compton scattering are presented. For the first time, information about the orbital angular momentum of quarks in the nucleon can be extracted from experiment. Using a new detector for recoil particles, HERMES will be able to give even more complete results in future.

1. The structure of the proton

In previous decades high energy experiments focussed on inclusive and semi-inclusive measurements in deep inelastic scattering to reveal the internal structure of the nucleon. Flavour tagging and spin polarization allowed to extract the spin dependent parton distribution functions $\Delta q(x)$ for each quark flavour q separately as shown e.g. in the contribution by D. Hasch in these proceedings. In the previous years it became clear that certain aspects of the internal structure of the nucleon can only be accessed by hard exclusive scattering. A prominent example is the orbital angular momentum contribution L_q of quarks which contributes a significant fraction of the total spin 1/2 of the proton:

$$\frac{1}{2} = \frac{1}{2}\left(\Delta u + \Delta d + \Delta s\right) + L_q + J_g \qquad (1)$$

with J_g being the contribution by gluons. In hard exclusive reactions the experimentalist is confronted with two challenges: the cross sections at high energies are typically very small, demanding high luminosity machines and a large background suppression. Secondly the exclusivity condition requires a detection of all final state particles, in particular the recoil proton which has a momentum of typically only a few hundred MeV/c in a fixed target experiment. The HERMES experiment [1] was able to measure the reactions of hard exclusive meson production and deeply virtual Compton scattering (DVCS) and to obtain first information about the orbital angular momentum of quarks in the nucleon [2]. A recoil detector [3] that was installed in the last phase of the HERMES experiment improved the quality of the data that are currently being analysed.

2. Wigner functions and GPDs

In classical physics, a particle is completely defined by its position in phase space, i.e. by its position in coordinate- and momentum-space. A system of classical particles is described by a phase space distribution $f(x,p)$ and the evolution of $f(x,p)$ obeys the Boltzmann equation. Because of the uncertainty principle, in quantum mechanics a particle has no sharp position in phase space and phase-space distributions seem useless. Instead, complex wave functions describe quantum systems. Quantum systems are not completely determined, phases of wave functions have no absolute meaning and for square values of wave functions there is a probabilistic interpretation only. In 1932 Eugene Wigner managed to replace Schrödingers wave function by a distribution function $W(x,p)$ in phase space [4] according to

$$W(x,p) = \int_{-\infty}^{\infty} \Psi^*(x-\eta/2)\Psi(x+\eta/2)e^{ip\eta}\,d\eta. \qquad (2)$$

This Wigner function $W(x,p)$ is a real function. It contains the most complete information of the quantum system and can be used to replace the concept of the complex wave function from Schrödinger. In analogy, a Wigner *operator* can be introduced in quantum field theory in order to describe quarks in the nucleon. These Wigner operators correspond to multi-dimensional functions which contain the information of the phase space distributions of quarks in the nucleon. Experimentally, there is no way to access all degrees of freedom of the quarks at the same time. Therefore certain variables are integrated out (e.g. the transverse momentum distribution of the quarks) and what remains is called a *reduced* Wigner distribution with less variables. The Generalized parton distributions (GPDs) are an example of functions which are related to a reduced Wigner operator [5].

There are four twist-2 GPDs [6–8] for a proton for each quark flavour q: $H^q(x,\xi,t)$, $E^q(x,\xi,t)$, $\tilde{H}^q(x,\xi,t)$, and $\tilde{E}^q(x,\xi,t)$, where $x+\xi$ is interpreted as the longitudinal momentum fraction of the scattered quark, t is the t-channel momentum transfer squared, and 2ξ is the longitudinal momentum fraction which is transfered to the quark q (see Fig. 1). The skewness parameter ξ can be determined in the experiment from the Bjorken x_B according to $\xi = x_B/(2-x_B)$. A GPD can be interpreted as the probability amplitude that a nucleon emits a parton with a momentum fraction $(x+\xi)$ and re-absorbs it with $(x-\xi)$.

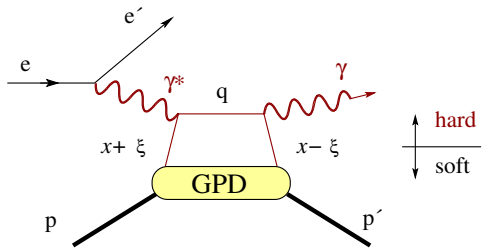

Figure 1. Diagram of deeply virtual Compton scattering. The emission and re-absorption of the quark in the nucleon is described by GPDs. The upper part of the diagram is a hard scattering process and described in pertubative QED and QCD.

GPDs can be interpreted a hybrid of an elastic form factor and a Feynman momentum distribution. When the parton momentum distribution x is integrated out, the GPDs become the ordinary Dirac and Pauli form factors of the nucleon

$$F_1^q(t) = \int_{-1}^{1} H^q(x,\xi,t)\,dx, \quad (3)$$

$$F_2^q(t) = \int_{-1}^{1} E^q(x,\xi,t)\,dx. \quad (4)$$

Hence they contain information about the (transverse) position distributions of the quarks in the nucleon. On the other hand, if the impact parameter is ignored (i.e. $t \to 0$), the ordinary polarized and unpolarized parton distributions are obtained in the forward limit

$$q(x) = \lim_{t\to 0} H^q(x,\xi,t), \quad (5)$$

$$\Delta q(x) = \lim_{t\to 0} \tilde{H}^q(x,\xi,t). \quad (6)$$

Note that the variable ξ disappears in both sets of equations above (because of the integration over all x in (3)-(4) and because of the symmetric forward limit in (5)-(6)). The limiting conditions (3)-(6) have been used to construct models for GPDs which respect existing experimental data on structure functions and form factors on the one hand and additional theoretical constraints (like the polynomiality condition of GPDs [9]) on the other hand. As GPDs describe correlations in phase space, it is not surprising that they contain information about the orbital angular momentum of quarks, just like the classical relation $L = r \times p$ implies. X. Ji revealed that the total angular momentum J^q of a quark q is related to GPDs [8] according to

$$J^q = \lim_{t\to 0} \frac{1}{2} \int_{-1}^{1} x\,[H^q(x,\xi,t) + E^q(x,\xi,t)]\,dx. \quad (7)$$

The orbital angular momentum L^q is obtained by subtracting the spin contribution Δq as measured in semi-inclusive DIS experiments $L^q = J^q - \Delta q$.

To conclude, the GPD formalism is a universal tool which allows parameterizing the non-pertubative structure of quarks (and gluons) in

a nucleon in a very general way. GPDs contain information about the momentum and spatial distributions of partons in the nucleon and give access to spin and orbital angular momentum.

3. The handbag diagram

In certain kinematical regions, hard exclusive reactions can be calculated using the QCD handbag diagram as shown in Fig. 1 for the process of DVCS and in Fig. 2 for hard exclusive meson production. It has been proven that the

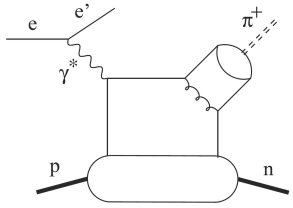

Figure 2. Description of hard exclusive meson production in terms of a QCD handbag diagram.

process factorizes for large Q^2 into a hard scattering process (upper part in Fig. 1) which is described by pertubative QED and QCD and a non-pertubative part (lower part of the diagram) which can be parameterized by GPDs. DVCS is the theoretically cleanest process to access GPDs. In hard exclusive meson production an additional form factor of the generated meson enters into the calculation of the diagram. Depending on the quantum numbers of the final state, different GPDs are involved. The production of vector mesons (ρ, ω, ϕ) is described by the polarization-independent GPDs H and E dominantly and the production of pseudoscalar mesons (π, η) involves mainly the polarization-dependent GPDs $\tilde{H}$ and $\tilde{E}$. DVCS (i.e. the production of a γ) depends on all four GPDs $H, \tilde{H}, E$ and $\tilde{E}$.

The DVCS process turns out to have a very small cross section at HERMES energies, much smaller than the Bethe-Heitler (BH) process which has the same final state as DVCS as shown in Fig. 3. At a first glance that seemed to make

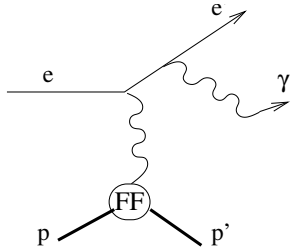

Figure 3. The diagram of the Bethe-Heitler process, which interferes with the DVCS handbag diagram.

it impossible to access DVCS at HERMES. However, there is an interference contribution I in the cross section which is enhanced by the large BH contribution and gives the opportunity to study DVCS at the amplitude level:

$$d\sigma \sim |T_{\mathrm{DVCS}}|^2 + |T_{\mathrm{BH}}|^2 + I \tag{8}$$

with

$$I = T_{\mathrm{DVCS}}\, T^*_{\mathrm{BH}} + T^*_{\mathrm{DVCS}}\, T_{\mathrm{BH}}. \tag{9}$$

Non-zero azimuthal asymmetries are the tool to access the DVCS amplitudes and the GPDs.

4. DVCS azimuthal asymmetries

The HERMES experiment was in the unique situation of having longitudinal beam polarization, longitudinal or transverse target polarization, and beams of either charge state, positrons or electrons. Azimuthal asymmetries are defined with respect to the angles ϕ and ϕ_S as shown in Fig. 4 and measured with low systematic uncertainties by flipping the target or beam polarization or the sign of the beam charge. In the following an experiment with unpolarized beam, transverse target polarization, and both beam charge states will be described. The azimuthal dependencies in the angles ϕ and $\phi - \phi_S$ of the cross section from Eq. 8 can be decomposed in Fourier

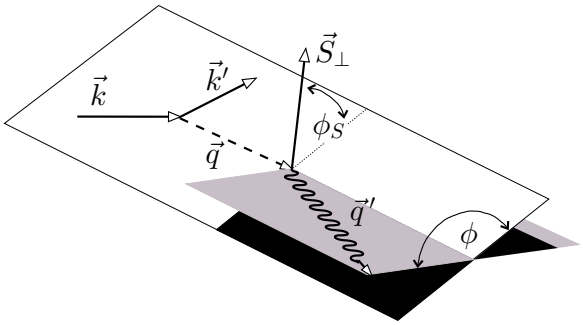

Figure 4. The azimuthal angle ϕ is defined as the angle between the scattering plane of the lepton and the production plane of the real photon with the virtual photon in the common z-direction. The angle ϕ_S corresponds to the orthogonal target polarization component in the nucleon rest frame.

coefficients separately for the BH, the DVCS and the interference term. Some of the terms change sign when the target polarization is flipped, some change sign when the beam charge is flipped, and some change sign when both are flipped at the same time. The measured yield N depends on the unpolarized cross section σ_{UU}, on the asymmetries A_{UT} with unpolarized beam and transversly polarized target from DVCS and from the interference part I, on the charge asymmetry A_C, on the transverse target polarization $S_\perp$, the lepton charge e_l and the azimuthal angles ϕ and ϕ_S according to

$$N \sim \sigma_{UU}[1 + S_\perp A_{UT}^{DVCS}(\phi, \phi_S) + \quad (10)$$
$$e_l S_\perp A_{UT}^{I}(\phi, \phi_S) + e_l A_C(\phi)]. \quad (11)$$

The three asymmetries A_{UT}^{DVCS}, A_{UT}^{I} and A_C in the above equation can be separated by flipping the target polarization and the beam charge independently. Experimentally the analysis is performed by a common likelihood fit of all relevant Fourier coefficients for all measured asymmetries simultaneously. The Figures 5 and 6 show the results for the most relevant Fourier coefficients of the charge and target spin asymmetries.

5. Orbital angular momentum of quarks

For many decades it was unclear how the orbital angular momentum of quarks can be accessed experimentally. It was even unclear how it can be consistently defined in a relativistic field theory. A break through was achieved by the investigations of X. Ji who defined the angular momentum such that it can be accessed by GPDs according to Eq. (7). An exact determination of J^q for up- and down-quarks requires a measurement of $H^q(x,\xi,t)$ and $E^q(x,\xi,t)$ over a broad range of x and ξ for small t. It is clear that the first pioneering experiments on GPDs are not able to do so. In a simplified approach a GPD model is fitted to the measured DVCS asymmetries. The model is chosen such that it fulfils the boundary conditions from theory and from other experiments (i.e. it reproduces the known $q(x)$, $\Delta q(x)$, $F^q_{1,2}(t)$). Such a model dependent approach gives first ideas about the angular momentum J^q and especially about the sensitivity of the DVCS data to this quantity. Fig. 6 shows predictions of a GPD model from M. Vanderhaeghen et al. [10] for three different values of the up-quark total angular momentum ($J^u = 0.2, 0.4, 0.6$) and for a vanishing down-quark total angular momentum ($J^d = 0$). The values of J^u and J^d are correlated and a fit yields

$$J^u + J^d/2.8 = 0.49 \pm 0.17_{exp} \quad (12)$$

in this model dependent analysis. By including data from a DVCS experiment on the neutron at Jlab [11], a second linear independent band can be defined as shown in Fig. 7. As a result, the total angular momentum of up- and down-quarks in the proton comes out to be on the order of $J^u = 0.4$ and $J^d = 0.15$ at a scale of about 2 GeV^2. This result is consistent with lattice calculations [2].

In a recent publication A.W. Thomas has shown that these results are also consistent with simple model assumptions of the nucleon [12]. He calculates the orbital angular momentum contributions L^q from the total angular momentum J^q at a very small scale of about 0.4 GeV^2 and assumes that the contribution of gluons to the spin is small as indicated by recent experiments at

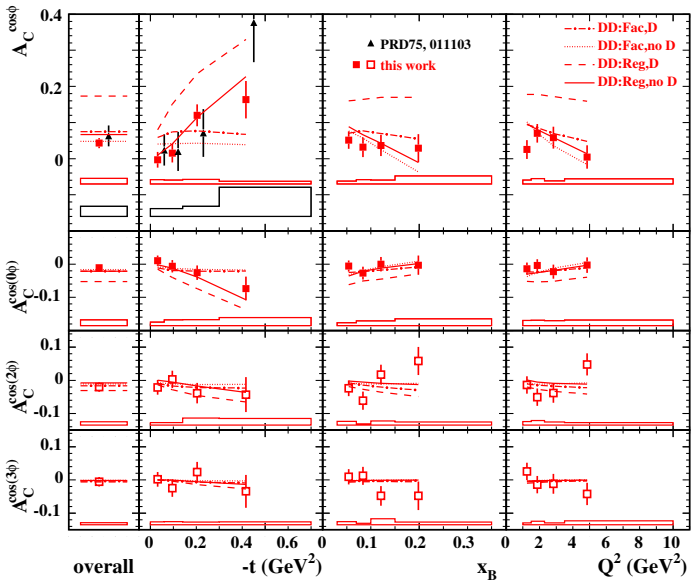

Figure 5. The extracted Fourier coefficients $A_C^{\cos n\phi}$ for the charge asymmetries of the interference term of BH and DVCS are shown as a functions of the kinematic variables. The value of $n = 0$ corresponds to the constant term. The $\cos\phi$ term has the most significant non-zero asymmetry. The points denoted as *this work* correspond to the recent HERMES publication [2]. The fits correspond to variations of a GPD model from [10]. See [2] for details.

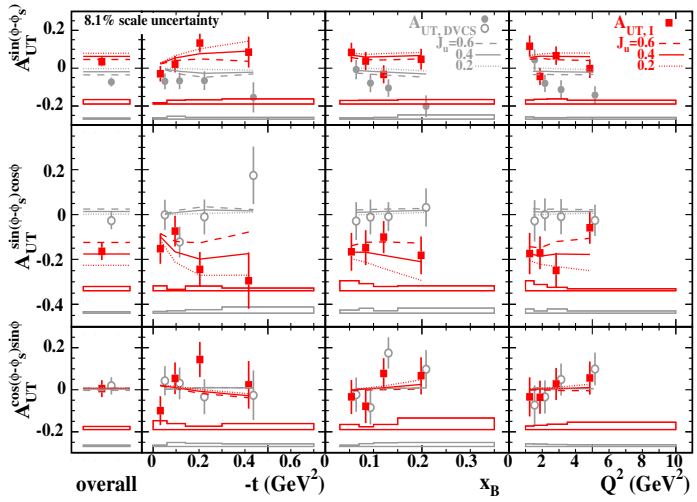

Figure 6. The extracted Fourier coefficients A_{UT} for the target spin asymmetries of the DVCS term and of the interference term are extracted separately. Several coefficients are plotted here as a function of kinematic variables. The circles (squares) correspond to the results for the DVCS (interference) term. The fits correspond to variations of a GPD model from [10] for various values of the up quark angular momentum. See [2] for details.

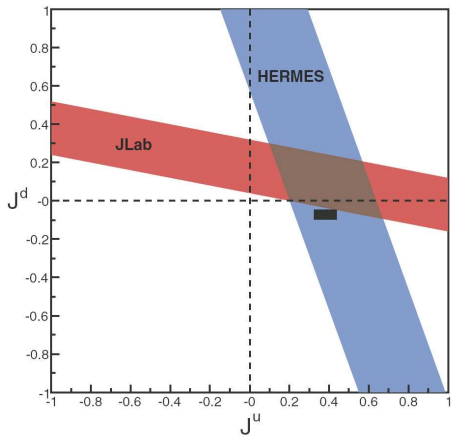

Figure 7. The results from HERMES and JLab constrain the total angular momentum of up- and down-quarks in the proton to values of about $J^u = 0.4$ and $J^d = 0.15$ at a scale of about 2 GeV^2 [12]. This result depends on the chosen GPD model. The black square is a result of a GPD independent model calculation from Myhrer and Thomas [12].

RHIC. As listed in Table 1, a most naïve non-relativistic model would associate the spin of the nucleon completely to the spin contribution of the quarks: $\Sigma = 100\%$. Due to the relativistic motion of quarks, a relativistic model reduces this contribution to about $\Sigma = 65\%$. The rest is assigned to the orbital angular motion. By assuming a simple one-gluon-exchange (OGE) hyperfine interaction, the contribution is further reduced. Finally, chiral symmetry, introduced by an effective pion cloud, leads to the final numbers in this model, yielding a spin contribution of $\Sigma = 38\%$ and a surprisingly large contribution of the orbital angular momentum of $L^{u+\bar{u}} = 50\%$ for the up-quarks and $L^{d+\bar{d}} = 12\%$ for the down-quarks. Even though, the entire results are consistent with recent data, one has to interpret them with great care as none of them are firm experimental results but only model dependent interpretations of the data. To obtain firm results on the orbital angular momentum of quarks, many more detailed measurements of the various GPDs must be carried out.

Table 1
The contribution of quark spins Σ and of orbital angular momenta L of up and down quarks to the total spin of the nucleon at a scale of 0.4 GeV^2 according to Ref. [12]. The successive lines show the results of adding a new effect to all the preceding effects: Simplest static quark model, relativistic motion of quarks, one gluon exchange hyperfine interaction and a non-pertubative pion cloud.

	Σ	$L^{u+\bar{u}}$	$L^{d+\bar{d}}$
Nonrelativistic	100%	0%	0%
Relativistic	65%	46%	-11%
OEG	50%	52%	-2%
Pion cloud	38%	50%	12%

6. The detection of the recoil proton

In the HERMES results shown above, DVCS events are selected by detecting the scattered lepton in the forward spectrometer and the real photon in the calorimeter. The exclusivity of the event is guaranteed only indirectly by requiring that no further particle is detected in the spectrometer and that the missing mass of the final state is consistent with the proton mass. Fig. 8 shows the missing-mass distribution of the HERMES data. The data within the vertical lines correspond to the selected exclusive BH and DVCS

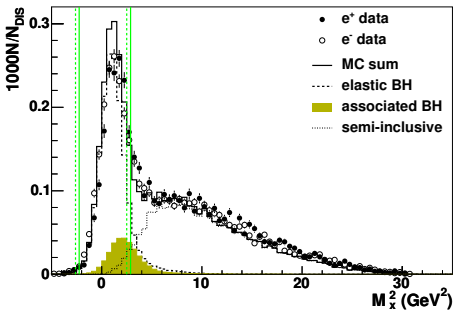

Figure 8. Distribution of the squared missing-mass from e^- and e^+ data and from Monte Carlo simulations. The vertical solid (dashed) lines enclose the selected exclusive region of the e^+ (e^-) data. The Monte Carlo curves show the background from the semi-inclusive and the associated Bethe-Heitler events to the elastic BH events.

data sample. From Monte Carlo simulations the contamination of this sample with semi-inclusive events and associated BH events (i.e. events with a final state resonance instead of a nucleon) can be estimated.

In 2006 and 2007 HERMES took data with a newly installed recoil detector. The purpose of the recoil detector is to detect the recoiling proton to improve the exclusivity of the selected data sample and to improve the determination of kinematic variables, especially t [3]. In addition the recoil detector can be used to detect resonance production and backward fragmentation as well as spectator nucleons from a deuterium target.

The recoil detector has an inner part of silicon strip counters which reside inside the beam vacuum and can detect recoil protons down to kinetic energies of about 10 MeV. It consists of 16 double-sided sensors and is used for momentum reconstruction and particle identification. Around the two layers of silicon sensors there are two barrels of scintillating fibres outside a thin beam pipe (see Fig. 9).

Each barrel consists of two parallel layers and two stereo layers (at 10°) of 1 mm scintillating fibres that are read out by multi-channel photomultipliers. The scintillating fibre barrels are surrounded by a 1 T superconducting solenoid. The scintillating fibre tracker allows determining the momentum of the tracks and is also used for particle identification. Between the SciFi barrels and the magnet there is a photon detector that consists of three layers of a tungsten scintillator sandwich for the detection of photons especially from resonance production: $\Delta^+ \to p\pi^0 \to p\gamma\gamma$. In figure 10 first results on particle identification are shown. A clear separation of pions and protons can bee seen. All three subdetectors (silicon, fibres and photon detector) contribute to the particle identification of tracks using a likelihood method and so-called parent distributions of the individual detector types.

The analysis of the data from the recoil detector is currently in progress. About 38 (10) million deep inelastic events have been taken on a hydrogen (deuterium) target, which corresponds to about 41,000 (7,500) DVCS events. The data were taken with right- and left-handed longitu-

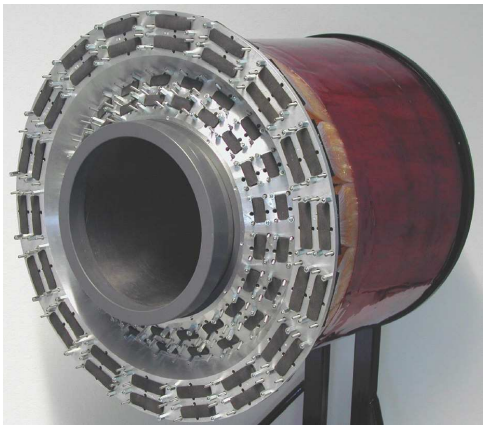

Figure 9. The scintillating fibre barrel that was build in Giessen consists of about 7000 fibres with 1 mm cross section that end on a connector plate. The light guide fibre bundles (not seen on the picture) are attached to the optical connectors and transport the photons about 4 m to about 4500 photomultiplier-pixels that are positioned outside the magnetic stray field of the detector.

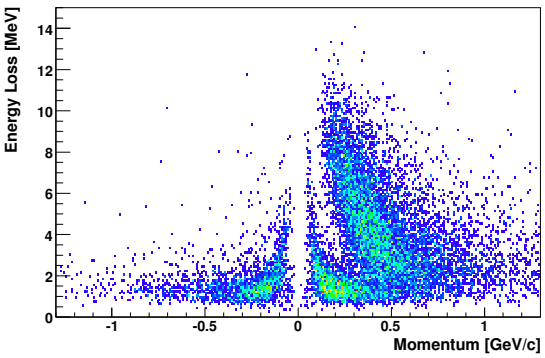

Figure 10. The energy deposit in the scintillating fibre detector is plotted versus the momentum of the particles in the recoil detector. Negative momentum values in this plot correspond to negative particles. There are clearly three bands seen which come from positive and negative pions and from protons.

dinally polarized positron and electron beams off an unpolarized target. We are looking forward for a large data sample of good quality.

7. Hard exclusive meson production

Hard exclusive meson production has been studied at HERMES in several channels. Here we will focus on the electroproduction of π^+ on a hydrogen target: $ep \to en\pi^+$. Experimentally the process is more difficult to extract compared to DVCS/BH as the background from non-exclusive processes is much larger. The only way to isolate the exclusive process without a recoil detection is by subtracting the $ep \to eX\pi^-$ process from $ep \to eX\pi^+$. In this case, the invariant mass distribution of the final state X shows an enhancement, but still no isolated peak at the invariant mass of the nucleon as shown in the upper panel of Fig. 11. The reason is that the π^+ background from semi-inclusive processes is larger than the π^- background. This has to be taken into account by Monte Carlo. After subtracting the PYTHIA Monte Carlo distribution of the corresponding difference of $\pi^+ - \pi^-$ from the HERMES data, an isolated peak at the nucleon mass is seen.

There are basically two ways to access this process by theory: the classical Regge formalism, which gives a good description of the data and the novel approach in terms of the QCD handbag diagram as in Fig. 2 where the process is described by GPDs. Fig. 12 shows the results for the differential cross section of exclusive pion production as a function of the variable $-t' = -(t-t_0)$, where t is the usual Mandelstam variable and $-t_0$ is the kinematically allowed minimum value of $-t$. Four bins in Q^2 are given. The dash-dotted lines in Fig. 12 show the leading-order calculations of the longitudinal part of the cross section computed by the GPD model from Ref. [10]. The model clearly underestimates the measured cross section. The solid lines show the same GPD model calculation after including power corrections due to intrinsic transverse momentum of partons and due to soft-overlap contributions. Now the model agrees in all four Q^2 bins with the data for $-t' < 0.3$ GeV^2. As the GPD model requires $-t' \ll Q^2$, it is not expected to agree with the data at large $-t'$. The Regge model [13] for $d\sigma/dt'$ (dashed lines) agrees with the HERMES data. The dotted lines show the contribution of the longitudinal cross section.

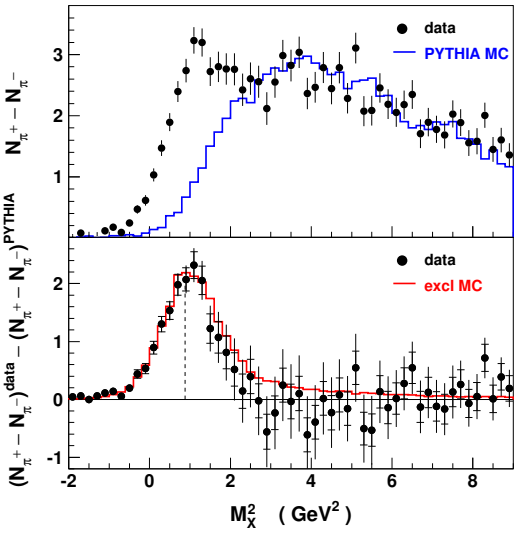

Figure 11. The upper panel shows the squared missing-mass distribution of the normalized yield difference of $N_{\pi^+} - N_{\pi^-}$ for data (points) and DIS Monte Carlo (histogram). The lower panel shows the double difference of the above data minus Monte Carlo results: $(N_{\pi^+} - N_{\pi^-})^{data} - (N_{\pi^+} - N_{\pi^-})^{MC}$. The dashed histogram represents the distribution from an exclusive Monte Carlo. The vertical dashed line indicates the squared mass of the neutron and coincides approximately with the measured mass peak.

8. Outlook

The HERMES experiment has done pioneering measurements on hard exclusive reactions and GPDs. Charge and single spin asymmetries have been measured in the interference term of DVCS and BH. First experimental results have been extracted that contain information about the orbital angular momentum of quarks in the nucleon. New data with high statistics have been taken at

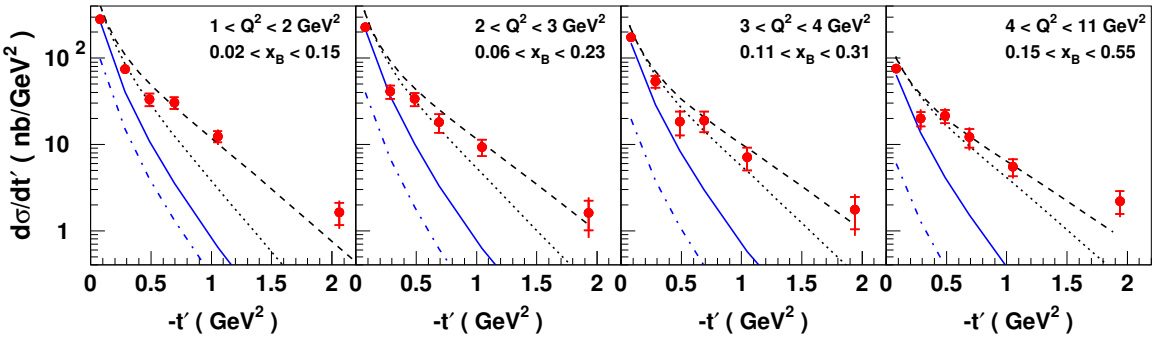

Figure 12. Differential cross section for electroproduction of exclusive π^+ as a function of $-t'$ in four Q^2 bins. The curves represent calculations based on a GPD model [10] for $d\sigma_L/dt'$ using a Regge-type ansatz for the t' dependence (dash-dotted lines: leading-order, solid lines: with power corrections) and a Regge model [13] for $d\sigma/dt'$ (dashed lines) and $d\sigma_L/dt'$ (dotted lines).

HERMES using a new recoil detector. The data are currently being analysed and are expected to improve the results statistically and systematically.

The study of generalized parton distributions in hard exclusive scattering is at its beginning, just as the study of the usual parton distributions started in the 1970s with the first inelastic inclusive scattering experiments. Many more experiments are needed to show the universality of the concept and to map out the GPD functions.

In the future PANDA experiment at FAIR several exclusive processes, especially the annihilation processes $p\bar{p} \to \gamma\gamma$ and $p\bar{p} \to \gamma\pi^0$ (see Fig. 13) will be studied [14], which are also described by the QCD handbag diagram and so-called Generalized Distribution Amplitudes (GDAs). The relation of GPDs and GDAs in these crossed diagrams will tell us about the universality of the new concepts.

Even at the LHC GPDs play an important role. Exclusive diffractive Higgs production (see Fig. 14) may be *the* way to determine the Higgs mass with much higher precision compared to inclusive measurements. Here generalized gluon distributions govern the diffractive cross section.

Even though there is an abundance of experiments that are related to GPDs, the only real way to map them out are lepton-nucleon scattering ex-

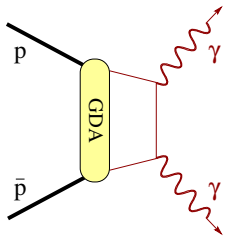

Figure 13. Description of the annihilation of $p\bar{p}$ into photons in terms of the QCD handbag diagram.

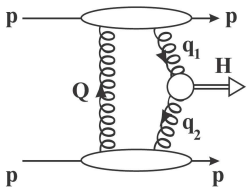

Figure 14. The 'exclusive' diffractive Higgs production is described by generalised gluon distributions.

periments. Any real progress in this field requires a new, polarized, high luminosity ep-collider. It is encouraging that after the premature shut-down of HERA there are new proposals for ep-colliders, as well in the US (EIC) as in Europe at FAIR.

REFERENCES

1. K. Ackerstaff *et al.* [HERMES Collaboration], Nucl. Instr. and Meth. A **417** (1998) 230.
2. A. Airapetian *et al.* [HERMES Collaboration], JHEP **06** (2008) 066.
3. HERMES Collaboration (R. Kaiser ed.), DESY PRC 02-01, HERMES Internal Note 02-033 (2002).
4. E.P. Wigner, Phys. Rev. **40** (1932) 749.
5. A.V. Belitsky, X. Ji and F. Yuan, Phys.Rev. D **69** (2004) 074014.
6. D. Müller *et al.*, Fortschr. Phys. **42** (1994) 101.
7. A.V. Radyushkin, Phys. Rev. D **56** (1997) 5524.
8. X. Ji, Phys. Rev. Lett. **78** (1997) 610; Phys. Rev. D **55** (1997) 7114.
9. X. Ji, J. Phys. G **24** (1998) 1181.
10. M. Vanderhaeghen *et al.*, Phys. Rev. D **60** (1999) 094017; Phys. Rev. D **62** (2000) 025501.
11. M. Mazouz *et al.* [Jefferson Lab Hall A Collaboration], Phys. Rev. Lett. **99** (2007) 242501.
12. A.W. Thomas, Phys. Rev. Lett. **101** (2008) 102003.
13. J.M. Laget, Phys. Rev. D **70** (2004) 054023.
14. M. Düren, "Proc. of the Xth Int. Conf. On Hadron Spectroscopy", Aschaffenburg, Germany (2003), AIP Conf. Proc. **717** (2004) 827.